Chinese Physics Letters

LETTER

Frequency-Dependent Spatial Regulation of Chiral and Antichiral Edge States in Photonic Crystals under Sublattice Modulation

Cite as: Yousi Chen *et al*. 2026 *Chin. Phys. Lett.* **43** 070401

Recommended Articles

Nuclear Matter in Relativistic Brueckner–Hartree–Fock Theory Using the Leading Order Covariant Chiral Interactions with Local and Nonlocal Regulators
Wei-Jiang Zou, Yi-Long Yang, Shihang Shen, and Jie Meng
Chin. Phys. Lett. **42**, 080101 (2025)

Chiral Pair Density Waves with Residual Fermi Arcs in RbV_3Sb_5
Xiao-Yu Yan *et al*.
Chin. Phys. Lett. **41**, (2024)

Localized Topological States in Finite Non-Hermitian Photonic Lattices
Xiong Fan, Wenchi Zang, Ming Ma, Li-Gang Wang, and Tianxing Ma
Chin. Phys. Lett. **43**, 040701 (2026)

Tunable Filtering of Orbital Angular Momentum Modes via Spatial Depth-Dependent Mode Transformation
Haisheng Wu *et al*.
Chin. Phys. Lett. **41**, 124203 (2024)

Manipulating the Spatial Structure of Second-Order Quantum Coherence Using Entangled Photons
Shuang-Yin Huang *et al*.
Chin. Phys. Lett. **41**, (2024)

Floquet Non-Abelian Topological Charges and Edge States
Jiaxin Pan, and Longwen Zhou
Chin. Phys. Lett. **42**, 090706 (2025)

A series journal of Chinese Physical Society distributed by IOP Publishing

Chinese Physics Letters

Chin. Phys. Lett. **43** 070401 (2026)

LETTER

DOI: 10.1088/0256-307X/43/7/070401
CSTR: 32039.14.0256-307X.43.7.070401

Frequency-Dependent Spatial Regulation of Chiral and Antichiral Edge States in Photonic Crystals under Sublattice Modulation

Yousi Chen(陈幼思)[1,†], Shangxian Du(杜尚贤)[1,†], Shiyu Liu(刘施语)[1,*], Weipeng Li(李伟朋)[1], Liwei Shi(石礼伟)[1], Enyuan Wang(王恩元)[2], and Yuting Yang(杨玉婷)[1,*]

[1]School of Materials and Physics, China University of Mining and Technology, Xuzhou 221116, China
[2]School of Safety Engineering, China University of Mining and Technology, Xuzhou 221116, China

[†]These authors contributed equally to this work.
[*]Corresponding authors. Email: ShiyuLiu@cumt.edu.cn; yangyt@cumt.edu.cn

The chiral edge states in the Haldane model and the antichiral edge states in the modified Haldane model have been extensively studied, revealing intriguing transport properties. In this work, the frequency-dependent spatial regulation of chiral and antichiral edge states is investigated in gyromagnetic photonic crystals through sublattice modulation. The unequal magnetization intensity on two-type sublattices, breaking the inversion symmetry, leads to the shift of the chiral edge state dispersions and the lifting of the degenerate antichiral edge states. Through simulations and experiments, we demonstrate that, under sublattice modulation, the transport efficiency of chiral and antichiral edge states at different edges is actively controlled, breaking through the functional limitations of conventional models. Based on this mechanism, a multi-channel waveguide is proposed, providing a new path for the functional innovation and system integration of topological photonic devices.

In the field of topological photonics, gyromagnetic photonic crystals provide a key platform for achieving backscattering-immune wave transport by breaking time-reversal symmetry. The renowned Haldane model demonstrated that introducing complex next-nearest-neighbor (NNN) hopping terms in a honeycomb lattice, without requiring a strong external magnetic field, can break the time-reversal symmetry of systems, thereby inducing a nontrivial topological phase [1–3]. The chiral edge states emerge within the complete band gap and propagate in opposite directions along the two parallel edges, which were experimentally confirmed in gyromagnetic photonic crystals at microwave frequencies [4–8] and applied to the development of various topological devices [9–17]. Subsequently, the modified Haldane model was proposed by setting the directions of NNN hoppings on the two sublattices to be identical [18]. The antichiral edge state dispersion curves of this model exhibit identical group velocity, where energy propagates in the same direction on both parallel edges. This modified Haldane model was quickly realized in multiple physical systems [19–31]. Topological photonic waveguides designed based on chiral and antichiral edge states exhibit significant robustness advantages compared to traditional waveguides, which are susceptible to defects, bends, and scattering. However, both the traditional Haldane model and the modified Haldane model in the photonic system indicate that, within a specific frequency range, the top and bottom edges can only simultaneously exhibit either chiral or antichiral transport modes, and both edges are constrained to operate within the same frequency band. This characteristic greatly limits the flexibility and functional density of waveguide designs.

This work systematically investigates the impact of sublattice modulation on the transport properties of the Haldane and modified Haldane models and obtains frequency-dependent spatial regulation of chiral and antichiral edge states. The difference in NNN hopping terms on two-type sublattices in the tight-binding model leads to unequal band gaps at the two valleys in the Haldane model and opened Dirac cones in the modified Haldane model. The dispersion curves of the edge states are deformed, inducing the shift of chiral edge state dispersion and the lifting of the degenerate antichiral edge state dispersion. The theoretical sublattice modulation is realized by tuning the magnetization intensity in gyromagnetic photonic crystals. The simulated and experimental results demonstrate that, under magnetization modulation, the frequency-dependent spatial separation of edge states is obtained, which breaks the limitation present in traditional models. Leveraging the coexistence of chiral and antichiral edge states, we propose a design scheme for a reconfigurable multi-channel topological waveguide, opening new avenues for integrated topological photonic devices.

The classic Haldane model, with broken time-reversal symmetry on the original graphene-like honeycomb lattice, as shown in Fig. 1(a), is defined by the Hamiltonian

$$H = t_1 \sum_{\langle i,j \rangle} c_i^\dagger c_j + t_2 \sum_{\langle\langle i,j \rangle\rangle} \mathrm{e}^{-\mathrm{i}v_{ij}\varphi} c_i^\dagger c_j + M \sum_i c_i^\dagger c_i,$$

where $c_i^\dagger$ (c_i) are the creation (annihilation) operators at site i; $\langle i,j \rangle$ and $\langle\langle i,j \rangle\rangle$ run over all nearest-neighbor (NN) and NNN hopping pairs, respectively. t_1 and t_2 are the NN and NNN hopping amplitudes, respectively, and φ represents the NNN hopping phase. M is the on-site potential energy. $v_{ij} = \pm 1$ indicates the hopping direction between sublattices A and B. The unequal NNN hoppings on the two sublattices break time-reversal symmetry, lift the degeneracy of the Dirac cones at the K and K' valleys, and open a full band gap. Two chiral edge states counter-propagate along the zigzag boundaries of the finite system described by the Haldane model. The modified Haldane model, as shown in Fig. 1(b), is achieved by setting the signs of v_{ij} for all NNN hoppings within sublattices A and B to be identical. In this case, the Dirac cones at the K and K' points do not split but shift relative to each other along the energy axis, forming a tilted band structure and giving rise to antichiral edge states that co-propagate along opposite system boundaries, while reverse transport compensation emerges in the bulk states propagating in opposite directions. The band structures of the chiral and antichiral edge states are displayed in

Received 10 April 2026; accepted 20 May 2026; published 28 July 2026
© 2026 Chinese Physical Society and IOP Publishing Ltd. All rights, including for text and data mining, AI training, and similar technologies, are reserved.

Check for updates

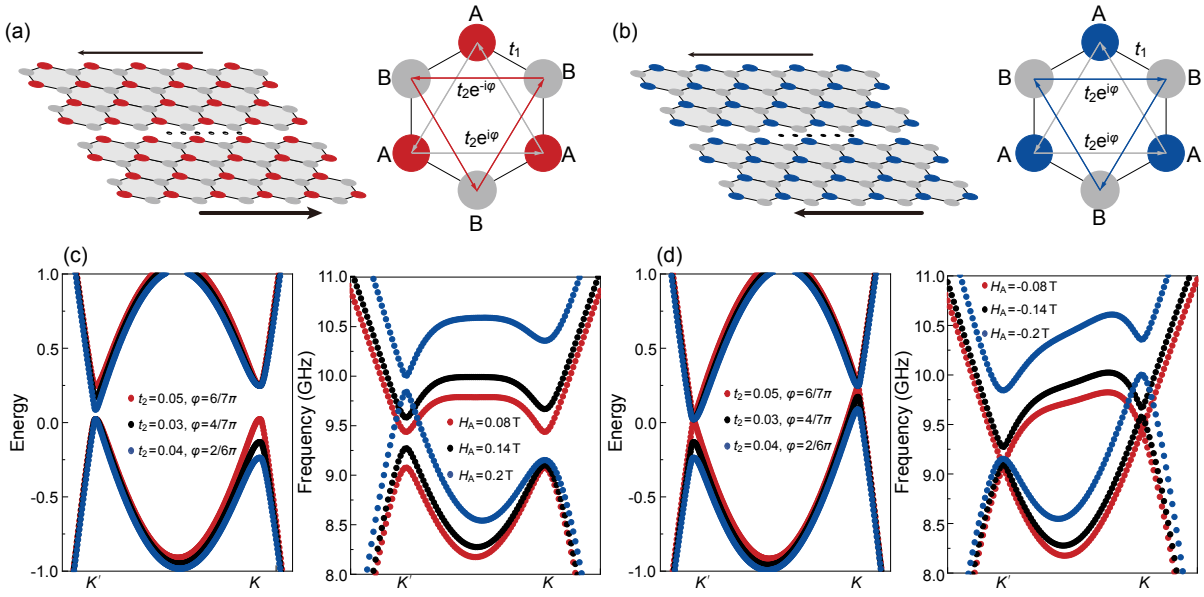

Fig. 1. Band evolution under sublattice-selective modulation. (a) and (b) Schematics of the tight-binding models for the Haldane model and the modified Haldane model. (c) Left panel: band evolution of the Haldane model with variation of the NNN hopping amplitude and phase on sublattice A. Right panel: photonic implementation of the Haldane model with variation of the magnetization intensity on sublattice A. (d) Band structures of the modified Haldane model in the tight-binding model and in photonic crystals. The NN hopping amplitude is $t_1 = 1$. The NNN hopping terms on sublattice B are fixed at $t_2 = 0.05$ and $\varphi = 6/7\pi$. The on-site energy is $M = 0$. The external magnetic field on sublattice B is fixed at 0.08 T.

Section S1 of the Supplementary Materials (SM).

By introducing sublattice-dependent NNN hopping phases φ_A and φ_B, the inversion symmetry of the Haldane model is broken. The Hamiltonian can then be written as

$$H = t_1 \sum_{\langle i,j \rangle} c_i^\dagger c_j + t_2^A \sum_{\langle\langle i,j \rangle\rangle} e^{-iv_{ij}\varphi_A} c_i^\dagger c_j + t_2^B \sum_{\langle\langle i,j \rangle\rangle} e^{-iv_{ij}\varphi_B} c_i^\dagger c_j.$$

The Bloch Hamiltonian after the Fourier transform is

$$H = \begin{pmatrix} H_A & H_0 \\ H_0^* & H_B \end{pmatrix},$$

where $H_0 = t_1 \sum_{i=1,2,3} e^{i\boldsymbol{k}\cdot\boldsymbol{\alpha}_i}$, $H_A = 2t_2^A \sum_{i=1,2,3} \cos(\varphi_A - \boldsymbol{k}\cdot\boldsymbol{v}_i)$, and $H_B = 2t_2^B \sum_{i=1,2,3} \cos(\varphi_B + \boldsymbol{k}\cdot\boldsymbol{v}_i)$. $\boldsymbol{\alpha}_i$ are the displacements from a B site to its three adjacent A sites, and $\boldsymbol{v}_1 = \boldsymbol{\alpha}_2 - \boldsymbol{\alpha}_3$, $\boldsymbol{v}_2 = \boldsymbol{\alpha}_3 - \boldsymbol{\alpha}_1$, $\boldsymbol{v}_3 = \boldsymbol{\alpha}_1 - \boldsymbol{\alpha}_2$. The on-site potential energy M is set to zero. The combined breaking of inversion and time-reversal symmetry allows the Dirac points to open unequal band gaps at the K and K' valleys in the Haldane model, leading to a tunable band structure, as shown in the left panel of Fig. 1(c). Sublattice modulation lifts the degeneracy of the Dirac points at the two valleys in the modified Haldane model, as shown in the left panel of Fig. 1(d).

The photonic implementations of the Haldane model and the modified Haldane model are realized using photonic crystals consisting of yttrium iron garnet (YIG) ferrite. The calculated photonic band structures are shown in Section S2 of the SM. The lattice constant is $a = 10$ mm, and the radius of the gyromagnetic cylinders is $r = 1.5$ mm. Under a static bias magnetic field H_0 along the z-axis, the relative permeability of the gyromagnetic material is a tensor

$$\mu = \begin{pmatrix} \mu_r & i\mu_k & 0 \\ -i\mu_k & \mu_r & 0 \\ 0 & 0 & 1 \end{pmatrix},$$

where $\mu_r = 1 + \frac{(\omega_0 + i\alpha\omega)\omega_m}{(\omega_0 + i\alpha\omega)^2 - \omega^2}$, $\mu_r = \frac{\omega\omega_m}{(\omega_0 + i\alpha\omega)^2 - \omega^2}$, $\omega_0 = \gamma H_0$, and $\omega_m = \gamma M_S$. H_0 is the applied external magnetic field, $M_S = 1860$ Gauss is the saturation magnetization, ω is the operating frequency, $\gamma = 1.76 \times 10^{11} s^{-1} \cdot T^{-1}$ is the gyromagnetic ratio, and $\alpha = 0.0002$ is the damping coefficient. For the Haldane model, we introduce sublattice modulation by fixing the magnetic field on sublattice B at 0.08 T and varying only the magnetic field strength on sublattice A. The difference in the NNN hopping terms between sublattices A and B arises from applying staggered magnetic fields of unequal magnitude but identical direction. The detailed band evolution in the tight-binding model is shown in Section S3 of the SM. As shown in the right panel of Fig. 1(c), when the external magnetic field H_0 on the A sites increases, the symmetry of the energy bands is broken, and an asymmetric band gap opens at the K and K' valleys in the Brillouin zone. In the modified Haldane model, we similarly introduce unequal sublattice modulation of the magnetization intensity, varying only the magnetic field on sublattice A. As shown in the right panel of Fig. 1(d), the originally degenerate Dirac cones gradually open a band gap as the magnetization intensity becomes unbalanced.

To demonstrate the transport properties of the chiral edge states under sublattice modulation, we perform microwave experiments on the photonic crystals, as shown in Fig. 2(a). To provide a controllable and uniform bias magnetic field along the z-direction on the gyromagnetic cylinders, we place two permanent magnets on the top and bottom surfaces of the gyromagnetic cylinders. The height d_2 of the permanent magnets is 1 mm, and the height d_1 of the gyromagnetic cylinders is 5 mm. To precisely fix their positions, the two permanent magnets are embedded into two parallel metal plates, each 4 mm in height. To further suppress microwave signal leakage in the vertical direction and ensure effective electromagnetic confinement for in-plane transport, we add additional metallic plates, each 1 mm in height, at the top and bottom. The top two metallic plates are pre-drilled with an array of small holes, each of radius 1 mm, to facilitate subsequent internal electric-field measurements. Two metallic blocks are placed along the zigzag boundaries of the photonic crystals to simulate perfect electric conductor boundaries. On the left and right sides, microwave-absorbing material is placed to maximize suppression of unwanted scattering.

The calculated band evolution of the chiral edge states in the tight-binding model and in photonic crystals is shown in Figs. 2(b) and 2(c). The numerical simulation software COMSOL Multiphysics is utilized to conduct electromagnetic simulations and band-structure analyses for the Haldane model under sublattice modulation. As displayed in the schematic, sublattice A is subjected to a strong magnetic field of 0.2 T (indicated in red), while sublattice B is subjected to a

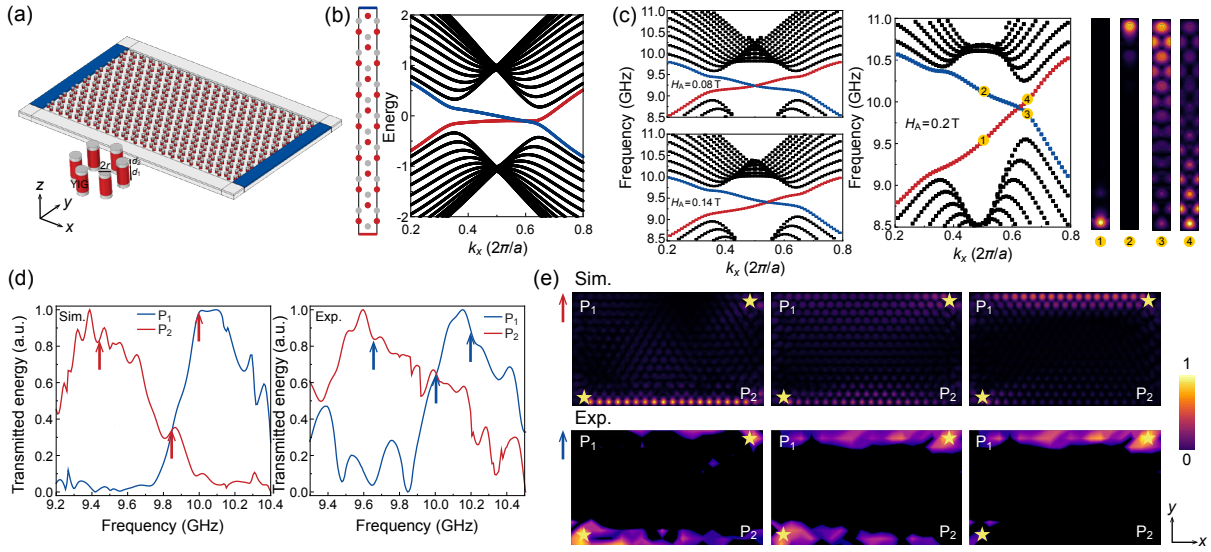

Fig. 2. Chiral edge states under sublattice modulation. (a) Schematic diagram of the experimental setup for observing chiral edge states. (b) Chiral edge-state dispersion in the tight-binding model. The shift of the chiral edge states induced by unequal sublattices A and B is indicated by red and blue lines. (c) Left panel: band structure of the chiral edge states with the variation of the magnetization intensity on sublattice A, for $H_A = 0.08$ T and 0.14 T. Right panel: $|E_z|$ eigen-electric-field distribution at different frequencies and wave vectors for $H_A = 0.2$ T. The magnetization intensity on sublattice B is fixed at $H_B = 0.08$ T. (d) Numerical simulations and experimental measurements of the transmission curves, with the upper and lower edges represented by blue and red, respectively. (e) The top and bottom panels show the electric field of the chiral edge states obtained from simulations and experiments, respectively. At different frequencies, indicated by the red and blue arrows in (d), the electric field intensities at the top and bottom edges are inverted.

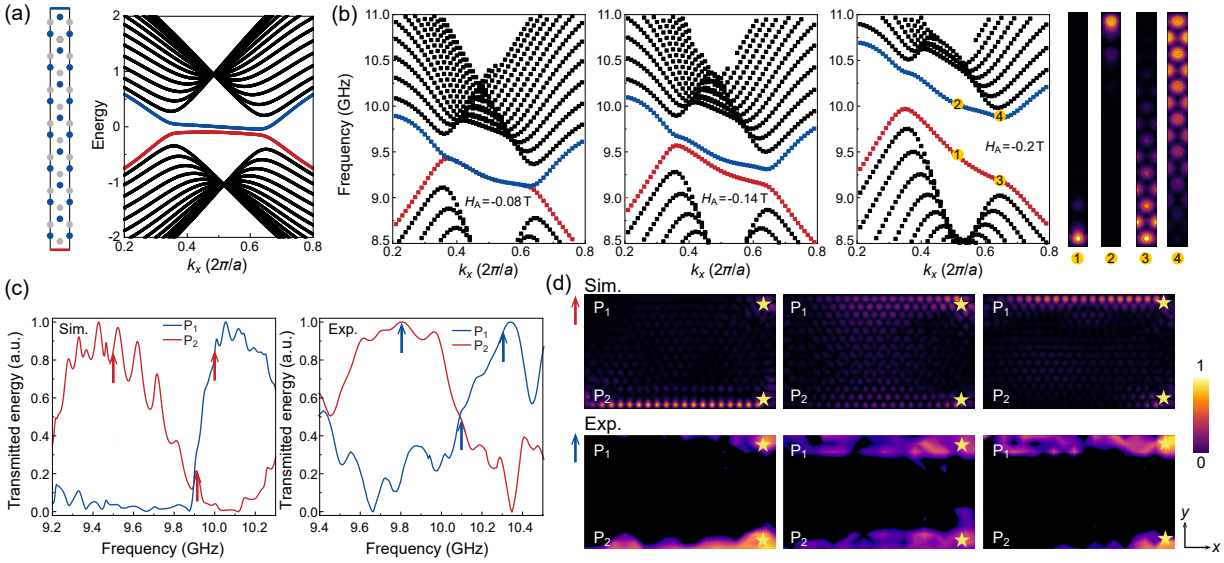

Fig. 3. Antichiral edge states under sublattice modulation. (a) Tight-binding model and band diagram of the antichiral edge states. The original degenerate antichiral edge-state dispersions are broken, induced by unequal sublattices A and B. (b) Band evolution of the antichiral edge states with the variation of the magnetization intensity on sublattice A, and $|E_z|$ eigen-electric-field distribution at different frequencies and wave vectors for $H_A = -0.08$, -0.14, and -0.2 T. The magnetization intensity on sublattice B is fixed at $H_B = 0.08$ T. (c) Numerical simulations and experimental measurements of the transmission curves, with the upper and lower edges represented by blue and red curves, respectively. (d) The top and bottom panels show the electric-field distributions of the antichiral edge states obtained from numerical simulations and experimental measurements, respectively, corresponding to the frequencies indicated by the red and blue arrows in (c). The yellow stars mark the excitation-source positions.

magnetic field of 0.08 T (indicated in gray). This unequal magnetic-field intensity between the two sublattices breaks the original symmetry and introduces an effective NNN hopping difference, causing the Dirac cones at the K and K' points to tilt significantly. Under this magnetization modulation, the system retains its nontrivial topological character; therefore, both the top and bottom edges support chiral edge states. The edge-state dispersions, indicated by blue and red lines corresponding to the top and bottom boundaries, respectively, show clear differences in group velocity and spatial localization. Their crossing point exhibits a significant shift in momentum space, directly reflecting the mapping of bulk-band tilting onto the edge states. For quantitative characterization of the transmission properties of the edge states in simulations and experiments, probes are placed at positions P_1 and P_2, yielding the transmission spectra shown in Fig. 2(d). The electric-field distributions of the chiral edge states at different frequencies are shown in Fig. 2(e), corresponding to the arrows in Fig. 2(d). At lower (higher) frequencies, the electric field propagating along the bottom (top) boundary is significantly stronger than that along the top (bottom) boundary, indicating that unequal sublattice magnetization intensity enables active control over the transmission efficiency of the respective boundaries. In the mid-frequency range, the electric-field intensities of the edge states at both boundaries are

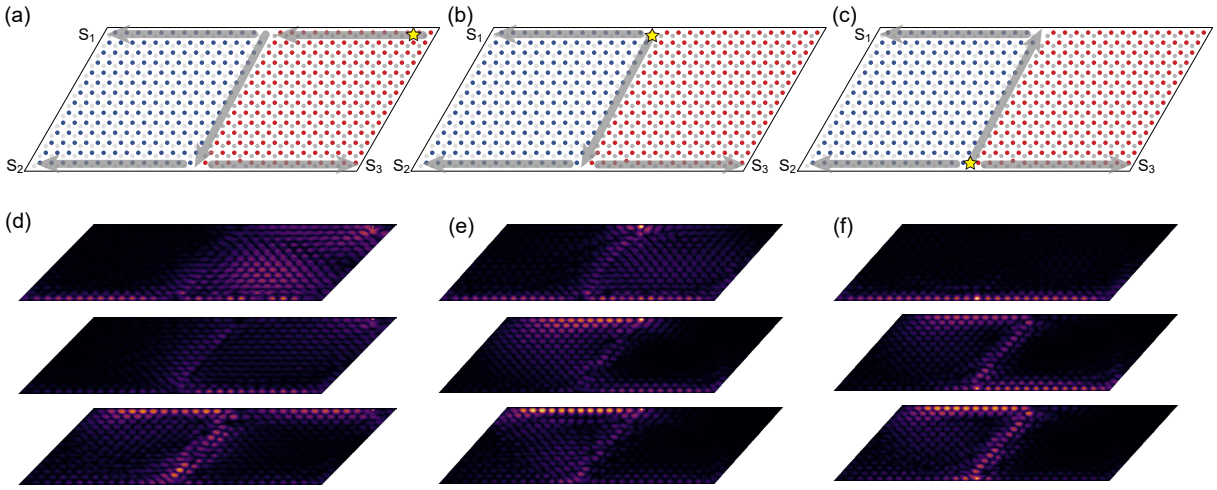

Fig. 4. Multi-channel waveguide. (a)–(c) Schematic diagram of the multi-channel unidirectional waveguide composed of two photonic-crystal structures supporting unequal propagation of chiral and antichiral edge states under sublattice magnetic-field modulation. The yellow stars indicate the positions of the excitation sources. (d) Electric-field distribution of the waveguide in (a) at 9.45, 9.70, and 9.48 GHz. (e) Electric-field distribution of the waveguide in (b) at 9.47, 9.87, and 10.00 GHz. (f) Electric-field distribution of the waveguide in (c) at 9.45, 9.89, and 9.92 GHz.

approximately equal. The experimentally measured electric-field distribution is highly consistent with the simulation results. The chiral edge states are immune to defects, indicating robust propagation, as shown in Section S4 of the SM. This method of achieving frequency-dependent, spatial regulation of chiral edge states through sublattice-selective magnetization provides a new degree of freedom for designing topological photonic devices.

Here, we conduct theoretical, simulated, and experimental analyses of the modified Haldane model under sublattice magnetic-field modulation. As shown in the schematic in Fig. 3(a), sublattice A is subjected to a reversed strong magnetic field of 0.2 T (indicated in blue), while sublattice B is subjected to a magnetic field of 0.08 T (indicated in gray). Figures 3(a) and 3(b) show the calculated dispersion curves of the antichiral edge states. It can be observed that the originally completely overlapping top- and bottom-edge-state dispersion curves open a band gap. The simulated and experimental results of the electric-field distributions and transmission spectra, as shown in Figs. 3(c) and 3(d), further reveal the frequency-dependent spatial regulation of the antichiral edge states. At higher (lower) frequencies, the electric field primarily propagates along the top (bottom) boundary, with its electric-field intensity significantly greater than that on the bottom (top) boundary.

The theoretical investigation and experimental verification of the chiral and antichiral edge states described above provide a key physical foundation for constructing multi-channel unidirectional waveguides. The transmission direction and efficiency of the edge states at different boundaries are regulated by the intensity and direction of the sublattice magnetic fields in gyromagnetic photonic crystals. As shown in Figs. 4(a)–4(c), the waveguides consist of two types of photonic crystals, supporting unequal propagation of chiral and antichiral edge states under sublattice magnetic-field control; their parameters are identical to those in Figs. 2 and 3. By adjusting the frequency of the excitation source and the direction and strength of the magnetic field, energy is emitted from different output ports, and the corresponding electric-field intensity distributions at different frequencies are shown in Figs. 4(d)–4(f). This highly reconfigurable capability not only overcomes the limitation of single-mode transmission in traditional waveguides but also enables integration of multimode and multichannel functionality, providing a new solution for high-density optical communication, optical signal splitting, and optical signal combining.

In conclusion, this study breaks through the limitation of dual-edge transport modes in the traditional Haldane and modified Haldane models by regulating the magnetization intensity on sublattices in photonic crystals, revealing frequency-selective regulation of chiral and antichiral edge states. Both simulation and experimental results confirm that this scheme enables frequency-differentiated distribution of chiral and antichiral edge states at different boundaries, providing fundamental physical support for multi-functional integration in photonic devices. The reconfigurable multi-channel waveguide, with the flexibility of magnetic field regulation and the robustness of transport modes, effectively enhances the design freedom of topological photonic devices. In the future, these research results can be extended to fields such as optical communication and integrated optics, laying a foundation for developing high-performance topological photonic chips.

Acknowledgements

This work was supported by the National Natural Science Foundation of China (Grant Nos. 12574477 and 52227901) and the Fundamental Research Funds for the Central Universities (Grant No. 2023ZDYQ11003).

References

[1] Haldane F D M 1988 *Phys. Rev. Lett.* **61** 2015
[2] Haldane F D M and Raghu S 2008 *Phys. Rev. Lett.* **100** 013904
[3] Raghu S and Haldane F D M 2008 *Phys. Rev. A* **78** 033834
[4] Wang Z, Chong Y D, Joannopoulos J D, and Soljačić M 2008 *Phys. Rev. Lett.* **100** 013905
[5] Wang Z, Chong Y D, Joannopoulos J D, and Soljačić M 2009 *Nature* **461** 772
[6] Fu J X, Liu R J, and Li Z Y 2010 *Appl. Phys. Lett.* **97** 041112
[7] Ao X Y, Lin Z F, and Chan C T 2009 *Phys. Rev. B* **80** 033105
[8] Poo Y, Wu R X, Lin Z F, Yang Y, and Chan C T 2011 *Phys. Rev. Lett.* **106** 093903
[9] Tang G C, Huang Y H, Chen J F, Li Z Y, and Liang W Y 2022 *Opt. Express* **30** 28762
[10] Chen J F, Qin Q M, Peng C Q, Liang W Y, and Li Z Y 2021 *Front. Mater.* **8** 728991
[11] Skirlo S A, Lu L, and Soljačić M 2014 *Phys. Rev. Lett.* **113** 113904
[12] Skirlo S A, Lu L, Igarashi Y, Yan Q H, Joannopoulos J, and Soljačić M 2015 *Phys. Rev. Lett.* **115** 253901
[13] Bahari B, Ndao A, Vallini F, Amili A E, Fainman Y, and Kanté B 2017 *Science* **358** 636
[14] Fang Y T, He H Q, Hu J X, Chen L K, and Zhang W 2015 *Phys. Rev. A* **91** 033827
[15] Chen J F, Liang W Y, and Li Z Y 2019 *Phys. Rev. B* **99** 014103
[16] Chen J F, Liang W Y, and Li Z Y 2020 *Opt. Lett.* **45** 4964

[17] Peng M, Wei Q, He A L, Huang Z H, Deng W Y, Liu Z Y, and Chen G 2025 *Phys. Rev. B* **112** 245411
[18] Colomés E and Franz M 2018 *Phys. Rev. Lett.* **120** 086603
[19] Mandal S, Ge R, and Liew T C H 2019 *Phys. Rev. B* **99** 115423
[20] Denner M M, Lado J L, and Zilberberg O 2020 *Phys. Rev. Res.* **2** 043190
[21] Bhowmick D and Sengupta P 2020 *Phys. Rev. B* **101** 195133
[22] Chen J F, Liang W Y, and Li Z Y 2020 *Phys. Rev. B* **101** 214102
[23] Zhou P H, Liu G G, Yang Y H, Hu Y H, Ma S L, Xue H R, Wang Q, Deng L J, and Zhang B L 2020 *Phys. Rev. Lett.* **125** 263603
[24] Yu L T, Xue H R, and Zhang B L 2021 *J. Appl. Phys.* **129** 235103
[25] Yang Y T, Zhu D J, Hang Z H, and Chong Y D 2021 *Sci. China Phys. Mech. Astron.* **64** 257011
[26] Chen J F and Li Z Y 2022 *Opto-Electron. Sci.* **1** 220001
[27] Xi X, Yan B, Yang L Y, Meng Y, Zhu Z X, Chen J M, Wang Z Y, Zhou P H, Shum P P, Yang Y H, Chen H S, Mandal S, Liu G G, Zhang B L, and Gao Z 2023 *Nat. Commun.* **14** 1991
[28] Liu J W, Shi F L, Shen K, Chen X D, Chen K, and Chen W J, and Dong J W 2023 *Nat. Commun.* **14** 2027
[29] Wang H F, Xie B T, and Ren W 2023 *Laser Photonics Rev.* **17** 2300764
[30] Xie L C, Jin L, and Song Z 2023 *Sci. Bull.* **68** 255
[31] Liu S Y, Yang Y T, Shi L W, Wang E Y, and Hang Z H 2025 *Photonics Res.* **13** 2688